






Article

Traction Synchronous Machine with Rotor Field Winding and Two-Phase Harmonic Field Exciter

Vladimir Prakht^{1,*}, Vladimir Dmitrievskii¹, Vadim Kazakbaev¹, Aleksey Paramonov¹
and Victor Goman²¹ Department of Electrical Engineering, Ural Federal University, 620002 Yekaterinburg, Russia² Nizhniy Tagil Technological Institute, Ural Federal University, 622000 Nizhniy Tagil, Russia; vvg_electro@hotmail.com

* Correspondence: va.prakht@urfu.ru

Abstract: Many modern electric drives for cars, trucks, ships, etc., use permanent magnet synchronous motors because of their compact size. At the same time, permanent magnets are expensive, and their uncontrolled flux is a problem when it is necessary to provide a wide constant power speed range in the field weakening region. An alternative to permanent magnet motors is synchronous motors with field windings. This article presents a novel design of a traction brushless synchronous motor with a field winding and a two-phase harmonic exciter winding on the rotor and zero-sequence signal injection. The two-phase harmonic exciter winding increases the electromotive force on the field winding compared to a single-phase one and makes it possible to start the motor at any rotor position. This article discusses the advantages of the proposed design over conventional solutions. A simplified mathematical model based on the finite element method for steady state simulation is presented. The machine performance of a hysteresis current controller and a field-oriented PI current controller are compared using the model.

Keywords: electric machines; design methodology; traction motorsAcademic Editors: Xinmin Li and
Liyan Guo

Received: 26 November 2024

Revised: 27 December 2024

Accepted: 3 January 2025

Published: 6 January 2025

Citation: Prakht, V.; Dmitrievskii, V.; Kazakbaev, V.; Paramonov, A.; Goman, V. Traction Synchronous Machine with Rotor Field Winding and Two-Phase Harmonic Field Exciter. *World Electr. Veh. J.* **2025**, *16*, 25. <https://doi.org/10.3390/wevj16010025>

Copyright: © 2025 by the authors. Published by MDPI on behalf of the World Electric Vehicle Association. Licensee MDPI, Basel, Switzerland. This article is an open access article distributed under the terms and conditions of the Creative Commons Attribution (CC BY) license (<https://creativecommons.org/licenses/by/4.0/>).

1. Introduction

Induction motors are a traditional solution for driving electric and hybrid vehicles, such as locomotives, trolleybuses, trams, cars, and trucks [1].

Traction drives that utilize an induction motor (IM) come with several notable disadvantages [2]:

- (1) Large losses and heating in the rotor: induction motors tend to generate significant losses and heat within the rotor, which can affect efficiency and performance;
- (2) Increased weight and size: compared to rare-earth permanent magnet synchronous motors (PMSMs) [3], induction motors are generally heavier and bulkier, which can be a drawback in applications where space and weight are critical factors;
- (3) Higher power rating of the inverter for wide constant power speed range (CPSR): when a wide CPSR is needed, the power rating of the inverter must be considerably higher. For example, the authors of [4] showed that a traction drive using an IM with a rated power of 50 kW and a CPSR of 3.5 requires an inverter with a rated power of 125 kVA. Another study [5] examining a traction IM with an output mechanical power of 50 kW and a CPSR of 4:1 also found the need for a 125 kVA inverter. This results in an inverter utilization factor of just 0.4 (50/125). If the CPSR is even wider, the utilization factor decreases further, reducing efficiency [1].

- (4) Temperature pulsations when parking on a slope: when a vehicle equipped with an induction motor is parked on a slope and the motor is used in electric brake mode at zero rotor speed, significant temperature pulsations occur in the traction converter switches. These fluctuations can shorten the lifespan of the inverter components [1,6]. To mitigate this, the rated power of the inverter must be significantly increased [7]. In contrast, synchronous machines can hold a vehicle on a slope at zero rotor speed using DC current in the stator phases, avoiding these temperature fluctuations. This ability to maintain constant temperature over the electric period without large fluctuations makes synchronous machines more reliable in this context.

The practical implications of these differences can be observed in various electric vehicles. For instance, earlier models like the Audi e-tron S and older Tesla models utilize induction motors [8,9]. In these vehicles, short-term parking on a slope, such as at a traffic light, is managed using a mechanical brake. However, users often find this less convenient than electric braking. Recognizing this, newer models, such as the Tesla Model 3 and Audi Q4 e-tron, switched from induction motors to synchronous machines, reflecting the advantages of the latter in terms of efficiency, size, and reliability in specific scenarios.

The majority of mass-produced electric vehicles from leading global manufacturers, including Toyota, Renault, BMW, Hyundai, General Motors, Ford, and KIA, utilize synchronous machines [8]. This trend indicates that modern synchronous drives are currently more promising than induction ones. However, several factors limit the widespread use of permanent magnet synchronous machines (PMSMs) in electric vehicles:

- (1) High cost of rare-earth permanent magnets (PMs): the cost associated with rare earth PMs remains a significant barrier.
- (2) Technological dependence: the reliance on a limited number of suppliers for rare earth elements creates a technological dependency that can affect production and supply chains.
- (3) Environmental impact: The extraction process for rare earth materials used in PMs has severe environmental consequences, making it a less sustainable option.
- (4) High-speed losses: At high rotational speeds, PMSMs experience large losses due to uncontrolled PM magnetic flux, especially with a wide constant power speed range (CPSR). This results in increased heating and a higher risk of magnet demagnetization.

Given these limitations, there is a growing interest in developing new traction motors that do not rely on permanent magnets and offer improved characteristics over induction motors. Electrically excited synchronous machines (EESMs) without permanent magnets are emerging as a promising technology to address these issues. EESMs have been adopted by leading European manufacturers, such as BMW and Renault, to reduce inverter power requirements, lower costs, and enhance reliability compared to induction motors [10,11].

EESMs feature an excitation winding on the rotor and often employ a brushless exciter [12,13]. While traditionally used as generators [12], recent advancements described their application in traction systems [13–15]. Companies like Mahle GmbH have begun serial production of these advanced electric machines, highlighting their potential in modern electric vehicle design [16].

The authors of [17] considered an EESM with controlled magnetic anisotropy, which can improve the performance of the EESM and allow the inverter utilization to be reduced.

In the work of [18], the EESM-embedded excitation system was considered by adding DC offset to the three-phase stator current.

Another article [19] and patent [20] considered the design of an EESM with a brushless harmonic exciter with a single-phase harmonic exciter winding (hereinafter simply “harmonic winding”), zero-sequence signal injection and a hysteresis stator current regulator. The disadvantages of this design include the following:

- The transfer of energy to the harmonic exciter winding does not occur effectively at all rotor positions. This reduces the magnitude of the electromotive force (EMF) at the output of the harmonic exciter and makes it impossible to start the motor at certain rotor positions.
- The slot sections of the harmonic winding coils placed in the slots of the field winding make a small contribution to the output EMF, which also reduces the efficiency of the harmonic exciter and complicates its design.
- To effectively transfer energy to harmonic winding, it is necessary that the angular size of the rotor sub-tooth is approximately equal to the pole pitch of the spatial third harmonic, and the entire rotor tooth is approximately equal to the period of the spatial third harmonic, that is, approximately 120 electrical degrees. This limits the possibilities for optimizing the design of a synchronous machine and achieving high efficiency.
- An inverter with a hysteresis current regulator is used to power the armature winding. This requires high-precision current sensors and fast switching transistors.

A similar single-phase harmonic winding design is also presented in [21].

To overcome the above-mentioned shortcomings of the known solutions, this article proposed a novel design of a synchronous machine with a multiphase harmonic exciter winding, presented in the application for an invention [22]. In the proposed design [22], multiphase winding is used, and the stator winding is effectively inductively coupled to the harmonic winding at any rotor position. This increases the efficiency of energy transfer to the field winding and allows the machine to start at any initial rotor position. In addition, in the proposed design, the slot parts of the harmonic winding coils are not placed in the slots of the field winding. Thus, all slot parts of the harmonic winding effectively create the excitation EMF, in contrast to the solution proposed in [19], in which the wires of the harmonic winding with opposite current direction are placed in the same slot of field winding and make a small contribution to the transformation of the harmonic flux component in the air gap into the harmonic winding EMF.

Moreover, the current study proposed a simplified computationally efficient vector-controlled HESM model for steady-state performance evaluation. Using the mathematical model, the characteristics of the Harmonic Exciter Synchronous Machine (HESM) are compared when using both a hysteresis current controller and a field-oriented current control (FOC). It is shown that the use of FOC current controller can significantly reduce the voltage required from the inverter and increase the inverter utilization factor, as well as significantly reduce current and torque ripples.

This article also presented a simplified mathematical model of a diode bridge rectifier connecting the harmonic winding and the field winding, which helps to avoid difficulties considering the nonlinear characteristics of diodes, which can be used for computer-aided optimization of the HESM.

2. Features of the Proposed HESM Design

In [19,20], an HESM design is considered, in which, to excite the machine, a zero-sequence signal is introduced into the neutral point of the armature winding, creating the third spatial harmonic of the magnetic field in a gap. This harmonic is picked up by the harmonic exciter winding on the rotor, rectified by a bridge rectifier and fed to the field winding. To make the harmonic winding, each rotor tooth near the gap is divided into two sub-teeth, onto which a single-phase harmonic winding is wound. As a result, one of the slot parts of the harmonic winding coil is placed in the slot of the field winding.

Figure 1a shows the HESM from [19] at the moment when the midpoints of the rotor teeth are located opposite to the midpoints of the phase zones of the stator winding.

According to Lenz's rule, the current in a harmonic winding tends to demagnetize the zero-sequence magnetic field in the stator winding. This current is rectified and powers the field winding. Figure 1b shows the same HESM at the moment when the midpoints of the rotor teeth are located opposite to the boundaries of the phase zones of the stator winding. In other words, there are no zero sequence currents opposite the middle of the rotor teeth, that is, there is no reason for the occurrence of induced current in the harmonic winding. Thus, energy transfer to the field winding is impossible. In intermediate rotor positions, energy transfer to the excitation winding is not carried out as efficiently, which reduces its excitation efficiency, leading to a decrease in the efficiency of the synchronous machine as a whole. In addition, it is difficult to start the machine with an arbitrary initial position of the rotor.

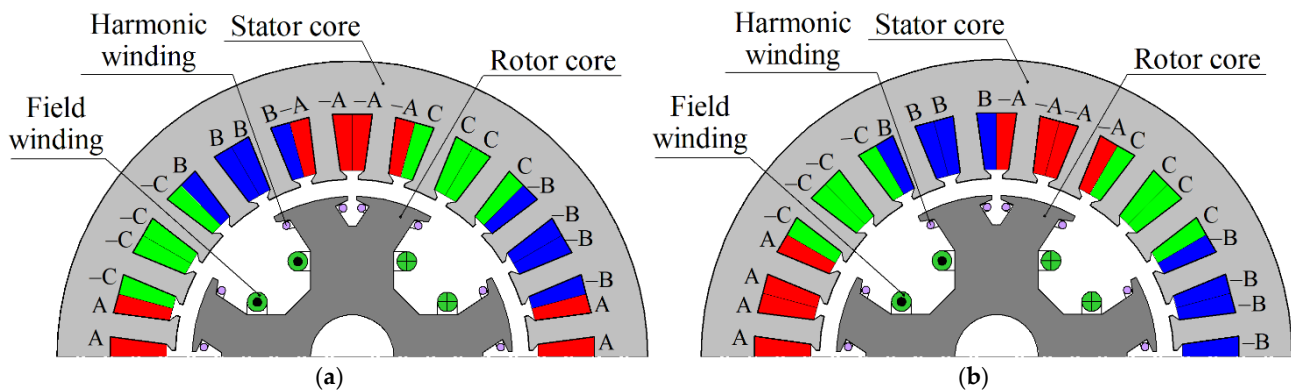


Figure 1. HESM design [18]: (a) aligned rotor position; (b) misaligned rotor position. The letters A, $-A$ (red), B, $-B$ (blue), C, $-C$ (green) indicate the phase zones of the stator winding.

In addition, in [19], in each rotor slot, along with the excitation winding, two slot sections of the harmonic winding, directed in opposite directions, are placed. However, the spatial change in the z-component of the vector magnetic potential occurs predominantly in magnetic cores and is practically absent in non-magnetic areas. As a result, the slot sections of the harmonic winding, placed in the slots of the field winding, are made opposite, balancing contributions to the EMF of the harmonic winding; that is, they do not lead to any significant result. Their location in the slot of the field winding complicates the design, reduces the space allocated for the field winding conductors, and, as a result, reduces the efficiency of the machine.

The fundamental harmonic (positive sequence) of the stator winding current is excited by a hysteresis current source, which provides a positive sequence sinusoidal current, greatly facilitating the modeling of the electrical circuit of the stator winding. However, the hysteresis current source requires high-precision, low-noise current sensors, and high-speed switches, which limits its application.

The injected zero-sequence current, due to the inevitable anisotropy of the rotor of a salient-pole machine, induces positive and negative sequence currents in the stator winding EMF, which, however, do not cause any additional currents, since the hysteresis current regulator has a high resistance for positive and negative sequences. Therefore, we represented the current in the stator winding in the form of two components: the positive sequence component injected by the three-phase hysteresis regulator, and a zero-sequence component injected by the zero-sequence injector.

This article proposed an improved alternative HESM design, as shown in Figure 2. This design was described in the application for the invention [22]. The machine has 4 poles, and the number of stator slots per pole and phase q is 4. The field winding and the harmonic winding are placed on the rotor. Figure 3 shows the layout of the harmonic

winding. Figure 4a shows the armature winding connection. As shown in Figure 4b, the harmonic winding and the field winding are connected to the rectifier. As a result, the voltage waveform from the harmonic winding is rectified and feeds the field winding. The presence of a two-phase harmonic exciter winding ensures a relatively constant inductive coupling between the stator winding and the harmonic winding and transfer of excitation energy to the rotor at any its position.

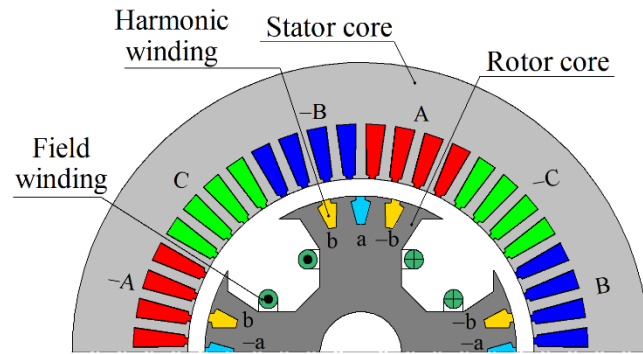


Figure 2. Sketch of the novel electric machine design (the size ratios do not correspond to the sizes adopted during modeling). The letters a, -a (light blue), b, -b (yellow) indicate the phase zones of the harmonic winding.

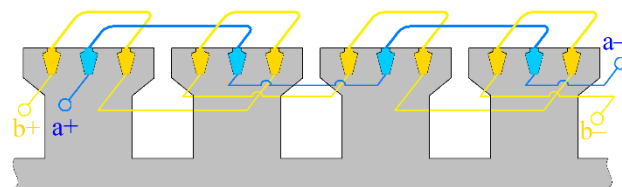


Figure 3. Sketch of rotor harmonic exciter winding layout. The coils are indicated by thick rounded lines at the top. The intercoil connections are shown below as thin lines. The letters a+, a- (light blue), b+, b- (yellow) indicate the phase zones of the harmonic winding.

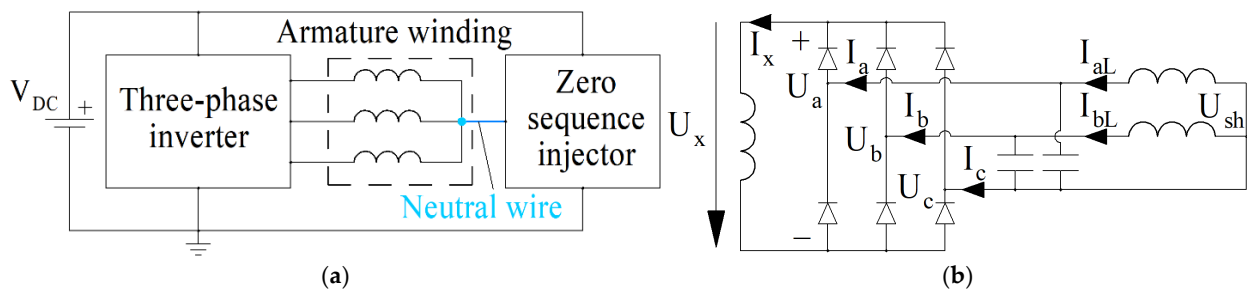


Figure 4. Motor winding connection: (a) stator; (b) rotor circuit and rotor voltages and currents, voltage levels U_a , U_b , U_c , and U_{sh} are shown relative to the lower negative rectifier bus.

In parallel with the harmonic winding, capacitors are connected to the diode bridge. Capacitors smooth out the voltage across the diode bridge. In addition, they compensate for the self-inductance of the harmonic winding, which increases the efficiency of energy transfer to the field winding.

3. Simplified Model of HESM Control System

Mathematical modeling of the proposed machine was carried out under the assumption of the widespread FOC strategy. In this case, the inverter impedance cannot be considered large, and it is necessary to consider the injected harmonics in the positive and negative sequence currents.

In our study, as well as in other similar papers [19,21,23] studying steady-state characteristics, the following assumptions were made to reduce the computational burden: the rotor speed is constant; amplitude of the stator current positive and zero phase sequences are fixed, and they are sinusoidal; the integral gains of PI current controllers are constant when using FOC. This allowed us to significantly speed up the transient process in the stator winding and obtain the steady state condition, spending less computing time.

Figure 5 shows a fragment of the simplest FOC control diagram. The reference for the currents in the rotating coordinate system I_{dq} and for the current in the neutral wire I_0 are supplied to the PI-controllers. The zero-sequence PI-controller generates a zero-sequence voltage reference, which does not require adjustment for rotation and is supplied to the injector. The I_{dq} PI-controller generates voltage u_{dq} without considering the rotational EMF (i.e., without taking into account cross connections). The rotational voltage ΔU_{dq} is added to the voltages u_{dq} . The full voltage U_{dq} reference is supplied to the $dq \rightarrow ABC$ converter.

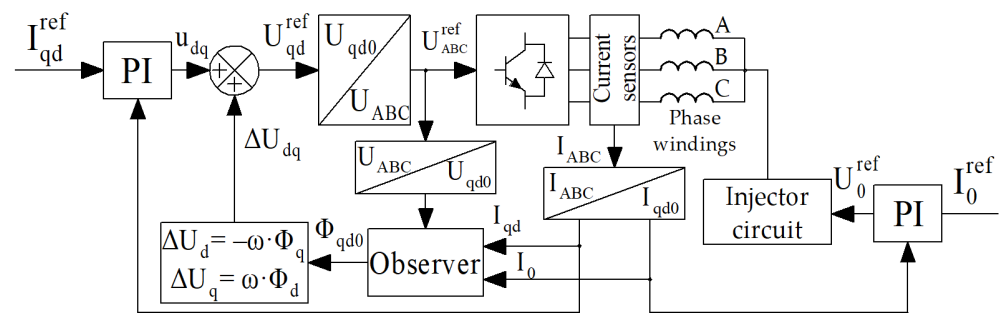


Figure 5. Control system diagram.

The robust scheme for calculating the motional EMF is based on determining dq -fluxes Φ_{dq} based on an observer by integrating the following:

$$\Phi_{dq} = e^{-i \cdot \Omega \cdot p \cdot t} \int (U_{dq} - R I_{dq}) \cdot e^{i \cdot \Omega \cdot p \cdot t} dt, \tag{1}$$

where Ω is the rotor angular frequency; p is the pole pair number; R is the armature phase resistance; i is the imaginary unit.

Note that the inverse conversion $ABC \rightarrow dq0$ can be applied not only to measured currents but also to phase voltages, since the direct conversion is carried out considering the voltage limitation. The stabilization of the observer is performed through additional feedback signals.

The equation for the stator electrical circuit has the following form:

$$\begin{aligned} \frac{d\Phi_{dq}}{dt} + R I_{dq} &= R_{dq}^{inv} (I_{dq}^{ref} - I_{dq}) + \int_{dq} i \\ \frac{d\Phi_0}{dt} + \frac{R}{3} I_0 &= R_0^{inv} (I_0^{ref} - I_0) + \int_0, \end{aligned} \tag{2}$$

where R_{dq}^{inv} , R_0^{inv} , \int_{dq} , and \int_0 are the proportional gains, as well as the integral gains of the PI current controllers for the dq -components and the zero sequence; I_0 is the zero-sequence current; I_{dq}^{ref} is the reference of the dq current; I_0^{ref} is the reference of the zero-sequence current; Φ_0 is the zero-sequence flux.

Let us simplify the equilibrium Equation (2) for the stator electrical circuit so as to obtain dynamics that correctly describe the steady-state condition. In steady state, the average current values are equal to their reference values. We assumed the integral part

of the PI-controller to be constant since they changed little in the electric period. These constants are obtained by averaging (2) as follows:

$$\int_{dq} = R_{dq} I_{dq}^{ref}, \int_0 = \frac{R}{3} I_0^{ref}. \quad (3)$$

Consequently, the equations of the stator electrical circuit take the following form:

$$\begin{aligned} \frac{d\Phi_{dq}}{dt} &= (R + R_{dq}^{inv})(I_{dq}^{ref} - I_{dq}); \\ \frac{d\Phi_0}{dt} &= (R_0^{inv} + \frac{R}{3})(I_0^{ref} - I_0). \end{aligned} \quad (4)$$

4. Features of the Diode Bridge Model

A separate problem in modeling the HESM is the modeling of the diode bridge, associated with the nonlinearity of its elements.

Connecting a voltage to an inductor instantly causes an increase in the current and the flux associated with it. The changing flux instantly causes a voltage surge in the circuits connected to this current. This reasoning is valid up to very high frequencies, at which the winding core practically does not exhibit high magnetic permeability due to the skin effect in electric steel sheets. Such reconstructions of the stator winding are typical for pulse-width modulation (PWM) power supply. In this study, it is assumed that the PWM frequency is sufficiently high, and the PWM voltage ripples in the harmonic winding are smoothed out by capacitors $C_h = 15 \mu\text{F}$. The electrical circuit of the rotor consists of a harmonic winding, capacitors, an excitation winding, and a rectifier. Equations relating currents and fluxes in the phases of the harmonic winding and in the field winding without considering the voltage drop across the diodes have the following form:

$$\begin{aligned} U_c - U_a &= \frac{d\Phi_a}{dt} + r \cdot I_{aL}; \\ U_c - U_b &= \frac{d\Phi_b}{dt} + r \cdot I_{bL}; \\ U_x &= \frac{d\Phi_x}{dt} + r \cdot I_x; \\ I_a &= I_{aL} - \frac{d(U_a - U_c)}{C_h \cdot dt}; \\ I_b &= I_{bL} - \frac{d(U_b - U_c)}{C_h \cdot dt}, \end{aligned} \quad (5)$$

where voltages and currents are designated in accordance with Figure 5. All voltages are measured from the negative node of the diode bridge.

The current balance at the input to the diode bridge has the following form:

$$I_a + I_b + I_c = 0. \quad (6)$$

A system of six pairs of Equations (5) and (6) has 10 unknowns: 6 currents $I_a, I_b, I_{aL}, I_{bL}, I_c, I_x$ and 4 voltages U_a, U_b, U_c . Fluxes are not independent variables, since for given currents, they can be found from the solution of the boundary value problem. Therefore, to close the system of equations, four more equations are required.

The transient problem is solved using Euler's backward method. At each step, for given states of the diode switches, a boundary value problem is solved. As a result of solving the boundary value problem, currents, fluxes, voltages, etc., are found. Based on the obtained solution, a new state of the diode switches is determined. Equations (5) and (6) contain derivatives of fluxes and voltages, which are approximated by finite differences. Their values in the previous step are used as additional inputs in this step.

The diodes included in the harmonic winding rectifier are extremely nonlinear elements, which can lead to divergence in the solution process. To overcome this difficulty, in this study, diodes of the rectifier are modeled not using their current–voltage characteristic

but as ideal switches. The description of the diode bridge model will consist of two parts: (A) description of the possible states of the diode bridge and the corresponding additional equations; (B) description of the algorithm for determining the state of the diode bridge in the next step.

4.1. Determination of Possible States of the Diode Bridge

Let us first consider these states without taking into account the voltage drops across the diodes. There are two operating states of the diode bridge:

- (1) The “through state” or short circuit state. A current flows through the field winding, supported by self-induction. All currents in the harmonic winding are less than the field current. The diodes are open through at least one column (two diodes connected in series). Therefore, all voltages on the diode bridge are zero; that is, we obtain the required additional four equations:

$$U_a = 0; U_b = 0; U_c = 0; U_x = 0. \quad (7)$$

We will encode this state with the flag $z = 1$. Other flags described below are not used in this state.

- (2) Working state. In this state, the voltage drop across the diode bridge is not zero. Some phases of the harmonic winding are connected to the field winding and power it. Each diode column $i = a, b, c$ (two diodes connected in series) can be in one of three states, encoded by flags $K_i, i = a, b, c$.

- $K_i = 0$, both diodes are closed, no current flows in the i -th circuit. $I_i = 0$.
- $K_i = 1$, upper diode is open, $U_i = U_x$.
- $K_i = -1$, lower diode is open, $U_i = 0$.

Thus, no matter what state the column is in, we have three equations, one for each column. The fourth equation can be obtained based on the balance of currents between the harmonic winding and the field winding as follows:

$$\sum_{i \text{ for which } K_i=1} I_i = I_x. \quad (8)$$

To complete the description of the model, consider the last condition, although atypical for the problem under consideration, when all the columns are closed. This happens, for example, when the voltage on the diode bridge is maintained by a capacitor connected in parallel with the field winding, which we do not consider in this study. In this case, $K_a = K_b = K_c = K_x = 0$ and $I_a = I_b = I_c = I_x = 0$. Then, the expression $I_a + I_b + I_c = 0$ turns out to be a consequence of the open circuit of the diode columns and, therefore, cannot be considered as an independent equation. Instead, the additional equation could be as follows:

$$U_{sh} = (\max[U_a, U_b, U_c] + \min[U_a, U_b, U_c])/2. \quad (9)$$

4.2. Description of the Algorithm for Determining the State of the Diode Bridge at the Next Step

The state of the diode bridge is determined by the following rules:

- In the short-circuit state ($z = 1$), the maximum module current $\max(|I_a|, |I_b|, |I_c|)$ flowing into the diode bridge is less than the rectified current. If this condition is violated, the short-circuit state is destroyed ($z = 0$). In this case, K_i takes values ± 1 in accordance with the sign of the corresponding current I_i .
- The rectified voltage is always positive. However, if, due to time discretization at some step, this condition is violated $U_x < 0$, then the operating state of the bridge $z = 0$ is no longer possible, and the short-circuit state $z = 1$ is switched on.

- In operating state $z = 0$, if the current flows through one of the diodes of the i -th column $K_i = \pm 1$, then K_i and I_i are always of the same sign. However, if, due to time discretization at some step, this condition is violated $K_i \cdot I_i < 0$, then current flow through the column is not possible, $K_i = 0$.
- The voltage on the stray (off) phase $K_i = 0$ in operating mode $z = 0$ is between 0 and U_x . However, if, due to time sampling at some step, this condition is violated, then the phase connects: $K_i = -1$, if $U_i < 0$; $K_i = 1$ if $U_i > U_x$.

The block diagram for calculating the new state of the diode bridge is shown in Figure 6.

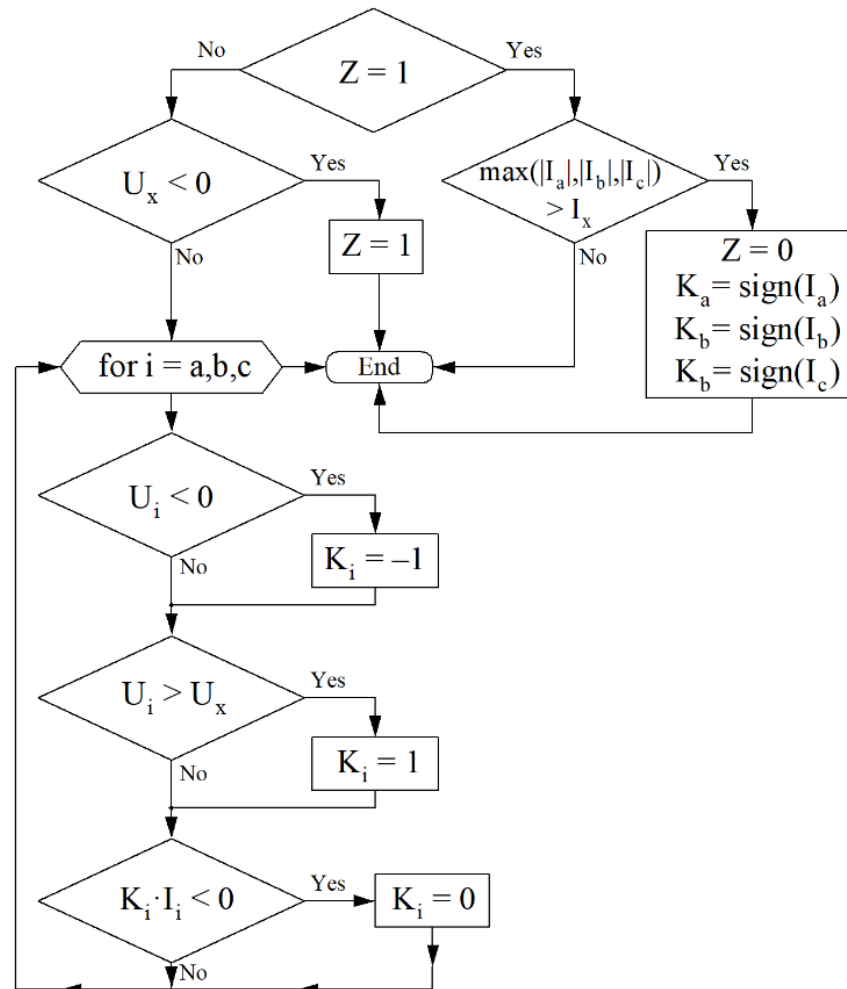


Figure 6. Rectifier condition calculation block-diagram.

To conclude our consideration of the diode bridge model, we note, whether in the short circuit or the operating state, when current flows through the field winding, it also flows through a pair of diodes, which allows us to consider the voltage drop across the diodes in the field winding circuit equation as follows:

$$U_x = d\Phi_x/dt + r \cdot I_x + 2\varepsilon, \quad (10)$$

where ε is the voltage drop across one open diode; U_x , I_x , and Φ_x are the voltage, current, and flux linkage of the field winding correspondingly; r is the field winding resistance.

5. Results of Mathematical Modeling

This section compares the simulation results with the FOC controller and the hysteresis current controller.

The modeling used an approach often used in theoretical studies of harmonic excitation systems of synchronous machines, in which the PWM component of the voltage is not considered, and the machine is modeled with specified stator phase currents. In this case, the phase current is set as the sum of the fundamental component of the current created by the main inverter and the high-frequency component generated by the injector [19,21].

During pilot modeling, it turned out that a hysteretic current source at the same injection current provides a more rapid increase in the field winding flux in the transient process. Therefore, the injection currents in the two strategies are selected to provide approximately the same rise rates for the excitation flux. The injection current for the hysteresis source is selected to be 60% of the current in the case of FOC compared to the hysteresis control. Table 1 shows the main motor design parameters. Figure 7 shows some of the main dimensions of the rotor. Table 2 shows some parameters of the HESM model.

Table 1. HESM design parameters.

Parameter	Value
Lamination length, mm	105
Stator outer diameter, mm	168
Stator inner diameter, mm	108
Air gap, mm	0.4
Stator yoke width, mm	16
Rotor pole pitch, mechanical degrees	90
Rotor pole angular dimension α , mechanical degrees	71
Angular distance between the slots of the harmonic winding β , mechanical degrees	30
Height of the excitation winding coil a_1 , mm	13
Width of the excitation winding coil b_1 , mm	15
Number of armature winding turns in slot	25
Number of field winding turns in coil	50
Number of harmonic winding turns in slot	3
Armature net copper fill factor	0.5
Stator slot area, mm ²	35.1
Field winding net copper fill factor	0.5
Field winding slot area, mm ²	195
Electric steel grade/thickness, mm	M270-35A/0.5

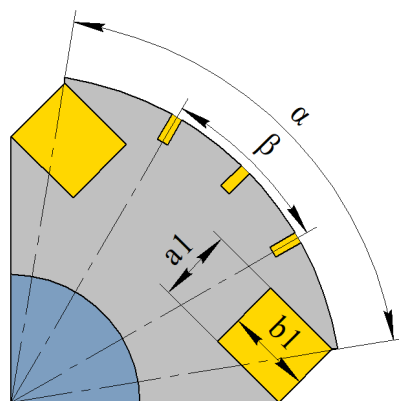


Figure 7. Some of the main dimensions of the rotor.

Table 2. Some parameters of the HESM model.

Parameter	Hysteresis Control	FOC
Armature phase current fundamental amplitude, A	5	
Amplitude of current injected into the neutral wire, A	2.1	3.5
Fundamental frequency, Hz	50	
Injection frequency, Hz	2000	
Proportional gain of dq -current controller R_{dq}^{inv} , Ohm	n/a	50
Proportional gain of neutral wire current controller R_0^{inv} , kOhm	1	
Number of time steps in one period of the third harmonic	200	
Voltage drop across two Schottky diodes in the diode bridge 2ε , V	0.6	

Figure 8 shows the calculated patterns of magnetic flux density and vector magnetic potential when using the hysteresis controller. Figure 9 shows the magnetic flux density and vector magnetic potential patterns when using the FOC controller. Areas of high saturation (magnetic induction greater than 2 T) are shown in white. Most parts of the magnetic circuit have low saturation levels.

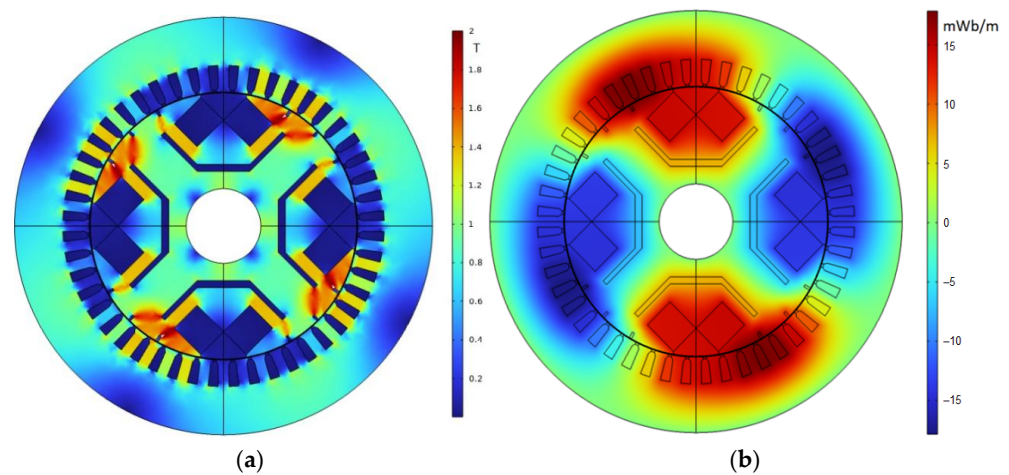


Figure 8. Motor simulation with hysteresis controller: (a) flux density; (b) magnetic vector potential.

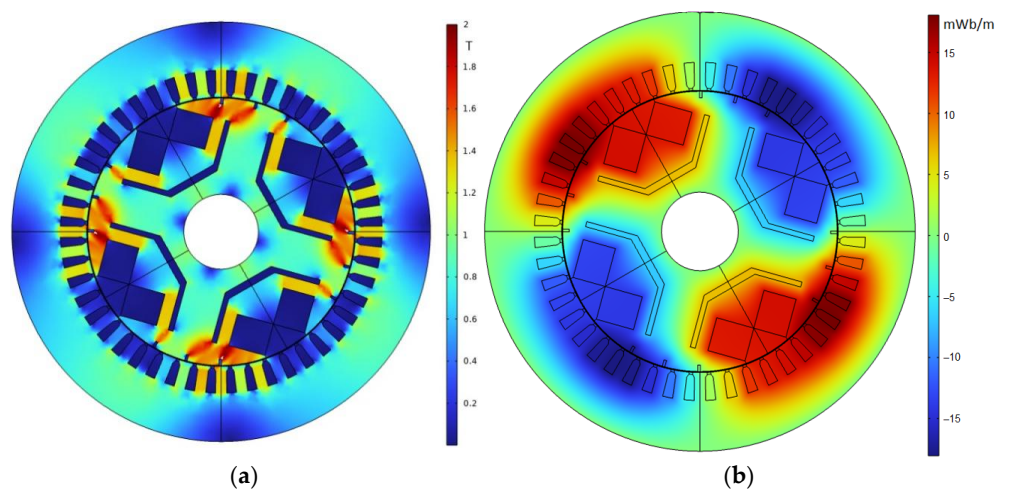


Figure 9. Motor simulation with FOC controller: (a) flux density; (b) magnetic vector potential.

Note that compared to the sketch geometry of the HESM shown in Figure 2, the rotor of the calculated geometry has an inner slot at each pole pitch. The presence of those slots is not essential for the operation of the HESM excitation system under consideration but only increases the rotor saliency, which may have a beneficial effect in the application under consideration, as explained in [17].

The slots of the harmonic winding have small dimensions, since they are supposed to accommodate only three turns, each of which consists of one conductor with a copper diameter of 0.6 mm.

The vector magnetic potential field varies slightly in non-magnetic regions. It changes most strongly in the areas of magnetic cores. This confirms the low efficiency of the slot sides of the harmonic winding, laid in the opposite direction in the field winding slots as in the design described in [18].

Figure 10 shows the excitation flux as a function of time over the entire simulation period. The excitation flux ripple is very low both when using the hysteresis controller and when using the FOC. The excitation flux values appear to be close not only at the beginning but also at the end of the transition process. Figure 11 shows the waveforms of the excitation current.

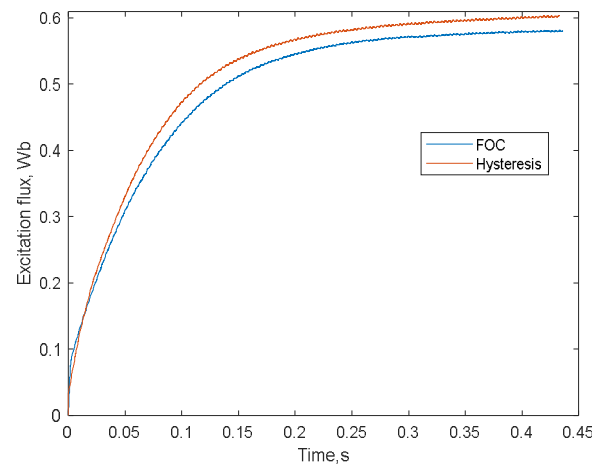


Figure 10. Excitation flux transient process.

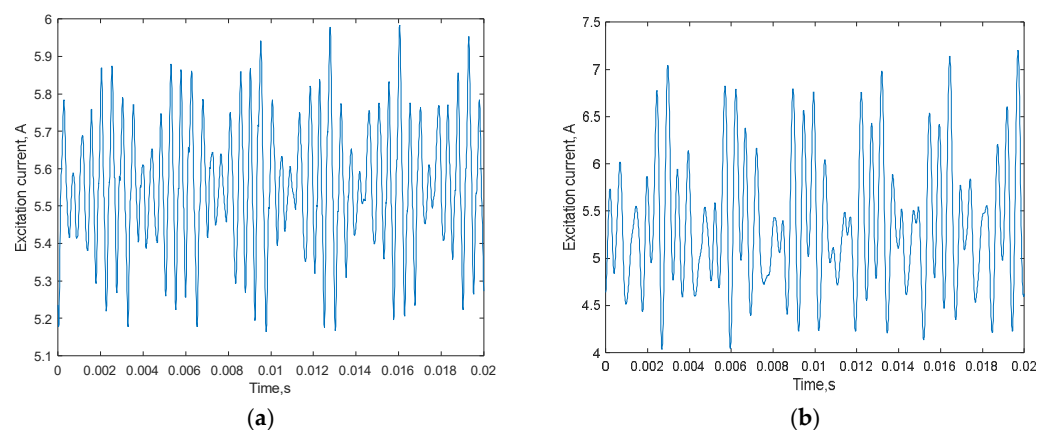


Figure 11. Excitation current: (a) hysteresis controller; (b) FOC controller.

Figure 12 shows the motor torque waveforms. It can be observed that the HESM torque ripple is higher than that of a typical wound field synchronous machine (WFSM) with slip rings because the HESM stator current consists of a zero-sequence excitation component in addition to the fundamental current component. This is a common disadvantage of WFSMs with brushless built-in excitation [19,21,23].

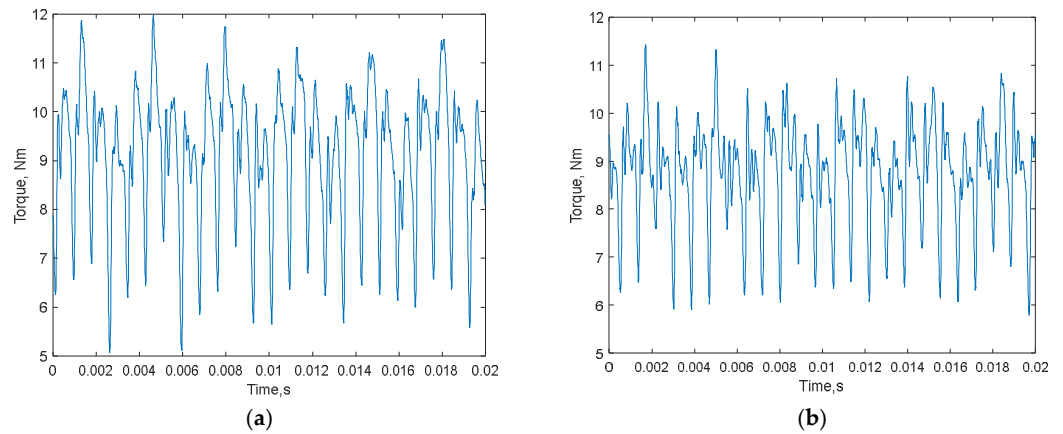


Figure 12. Motor torque: (a) hysteresis controller; (b) FOC controller.

Figure 13 shows the stator phase current waveforms. Figure 14 shows the neutral wire current waveforms. Figure 15 shows the phase voltage waveforms relative to the neutral. Figure 16 shows the line voltage waveform. Phase voltages have a significant injection component, and in line voltages (limited by the inverter), this component is significantly suppressed.

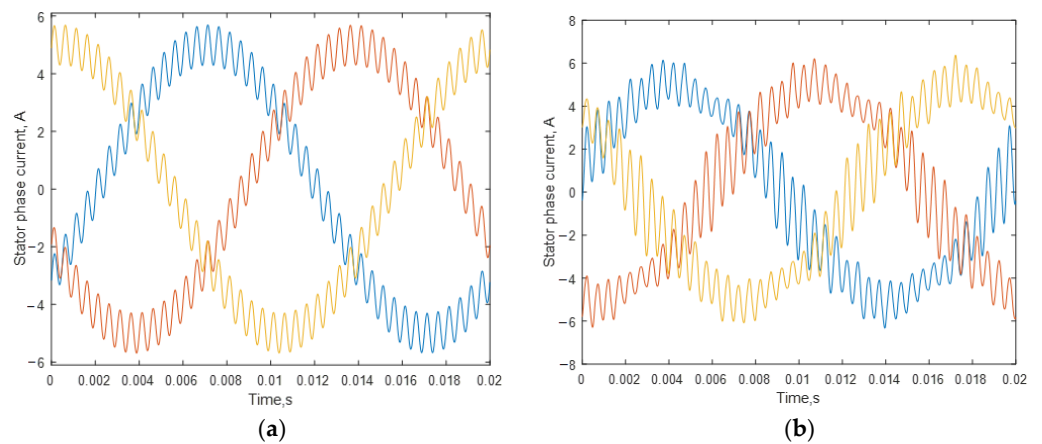


Figure 13. Phase current: (a) hysteresis controller; (b) FOC controller. The waveforms of currents of different phases are shown in different colors.

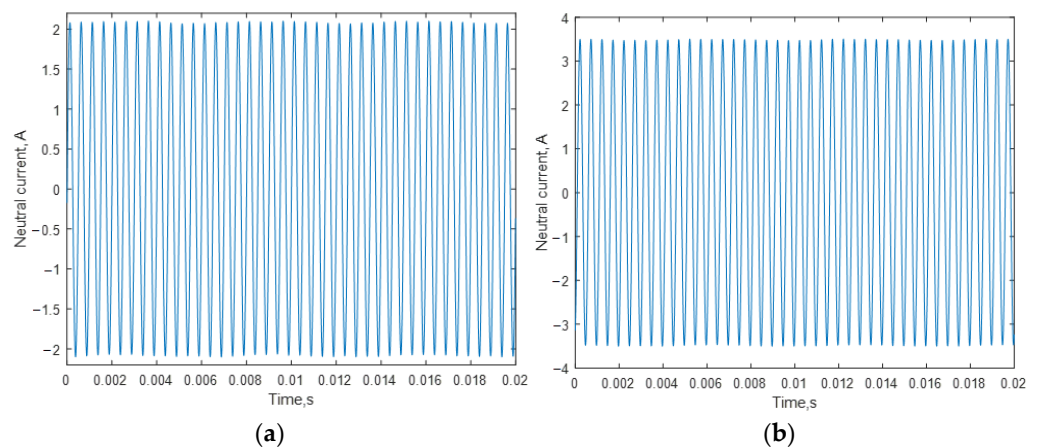


Figure 14. Neutral wire current: (a) hysteresis controller; (b) FOC controller.

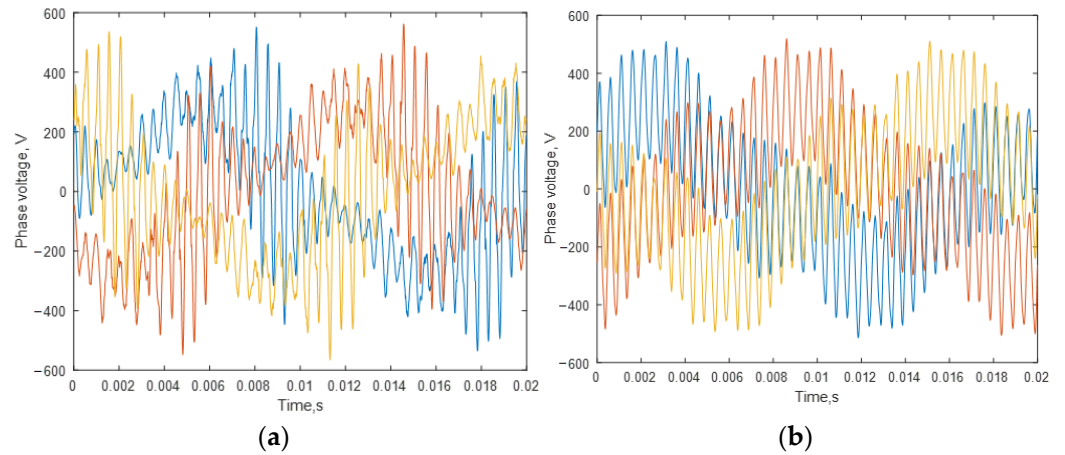


Figure 15. Phase voltage: (a) hysteresis controller; (b) FOC controller. The waveforms of voltages of different phases are shown in different colors.

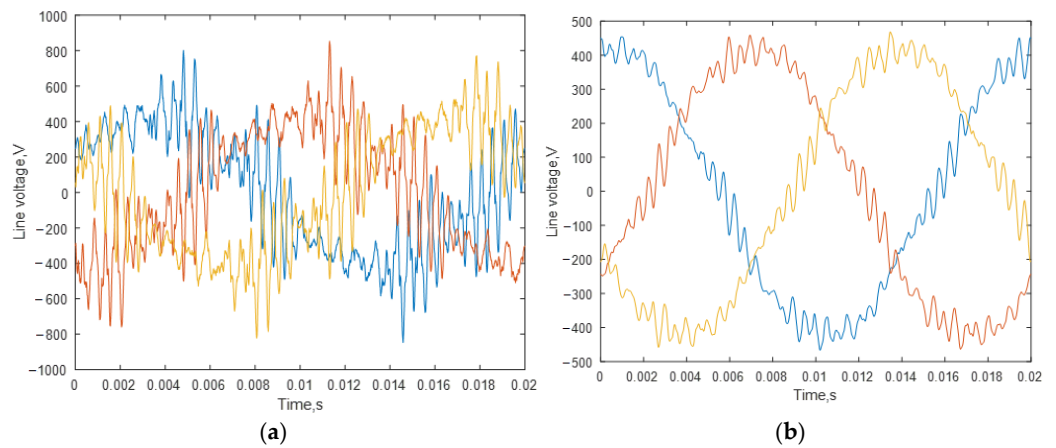


Figure 16. Line-to-line voltage: (a) hysteresis controller; (b) FOC controller. The voltage waveforms between different lines are shown in different colors.

Figure 17 shows the neutral voltage waveforms relative to the arithmetic mean phase voltage. These dependencies contain a high-frequency injected component and a third time harmonic excited by the fundamental harmonic due to the rotor anisotropy. The injected harmonic amplitude is 195 V and 142 V for the FOC and hysteresis sources, which are 17% and 42% of line-to-line voltage amplitude. Therefore, to reduce the rating of the injector transistors, the injected signal can be supplied through a step-down transformer. Table 3 shows the calculated motor performances.

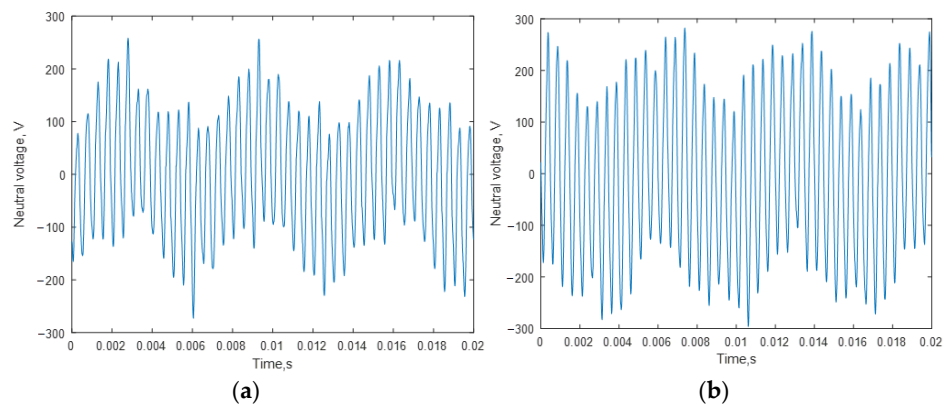


Figure 17. Neutral voltage relative to the arithmetic mean phase voltage: (a) hysteresis controller; (b) FOC controller.

Table 3. Simulation results.

Parameter	Hysteresis Control	FOC
Output mechanical power P_2 , W	1434.6	1376.9
Input electric real power P_1 , W	1578.8	1526.9
Armature copper loss, W	64.1	66.7
Stator steel loss, W	44.3	48.7
Rotor steel loss, W	9.5	9.8
Field winding copper loss, W	22.7	21.3
Diode loss, W	3.3	3.2
Harmonic winding loss, W	0.35	0.33
Line-to-line voltage amplitude, V	853	468
Line-to-line voltage RMS V_{rms} , V	337	299
Phase armature current RMS I_{rms} , A	3.57	3.64
Inverter apparent power, V·A	2082	1889
Power factor PF *	0.76	0.81
Torque ripple, %	76.0	64.4
Total loss, W	144.3	150.0
Efficiency η , % **	90.9	90.2
Field winding current, Ampere-turn	5.55	5.34

Note: * In this table, the power factor is calculated as $PF = P_1 / (\sqrt{3} \cdot V_{rms} \cdot I_{rms})$; ** the motor efficiency calculated as $\eta = P_2 / P_1$.

The iron losses presented in Table 3 are calculated using a conventional approach which is based on flux density waveform analysis considering magnetic core material properties [24]. These iron losses are approximately equal, both when using the hysteresis controller and with FOC.

Based on the calculations performed, we can conclude that the inductance of the excitation winding provides significant smoothing of the excitation flux and connecting a capacitor to the rectified voltage circuit for smoothing is not required. However, the ripple of excitation current has a large injection component. This is explained by inductive coupling between the armature and the field windings.

The FOC controller requires an injection current flowing in the neutral wire that is $100\% \cdot (3.5 - 2.1) / 2.1 = 66.7\%$ higher, and the efficiency is lower by $100\% \cdot (90.9 - 90.2) = 0.7\%$, but the line voltage is 100% less $(853 - 468) / 853 = 45.1\%$. The total apparent inverter power is $100\% \cdot (3729.6 - 2086.4) / 2086.4 = 44.1\%$ less. Torque ripple is also significantly reduced by $100\% \cdot (76 - 64.4) = 11.6\%$.

The higher efficiency of the HESM in the case of hysteresis control is explained by the very narrow hysteresis band. A similar assumption is made, for example, in [18]. Due to this, the current ripple is smaller than in the case of FOC. With a more detailed modeling of the control system and power electronics, other comparative results of hysteresis control and FOC in terms of current ripple and efficiency are possible.

The calculated torque ripple values do not differ significantly: 76% for the hysteresis control and 64.4% for the FOC control, respectively. These values are comparable with those reported for other HESMs presented in the literature [19,21].

The high line-to-line voltage with a hysteretic current controller is explained by the large injection component in voltage dq -component due to the anisotropy of the rotor. The injection component with FOC, although significantly smaller, is not eliminated.

6. Conclusions

This article presented a novel design of a traction synchronous motor with an excitation winding on the rotor with a two-phase brushless harmonic exciter, which increases the

efficiency of transferring the energy of higher harmonics of the stator magnetic field to the rotor to excite the machine, compared with the machine described in [19,20].

Also, the solution under consideration makes it possible to ensure that the machine starts in motor mode at an arbitrary rotor position, increases the inverter utilization factor, and reduces current and torque ripples.

The article used a mathematical model to analyze the characteristics of the electrical machine under consideration when using both the hysteresis current controller and the FOC PI-current controller. It is shown that in the case of the FOC PI-controller, more injection current is required, and the efficiency of the machine decreases. However, at the same time, the apparent inverter power is reduced by 44%, and the required voltage amplitude and torque ripple are also significantly reduced.

In future work, the authors plan to present a refined mathematical model of the considered HESM, develop a method for optimizing the HESM performances, including its torque ripple, and conduct experimental testing of the developed models.

Author Contributions: Conceptual approach, V.D. and V.P.; data curation, V.G. and V.K.; software, V.D. and V.P.; calculations and modeling, A.P., V.D., V.G., V.K. and V.P.; writing—original draft, A.P., V.D., V.G., V.K. and V.P.; visualization, A.P., V.D. and V.K.; review and editing, A.P., V.D., V.G., V.K. and V.P. All authors have read and agreed to the published version of the manuscript.

Funding: This work was supported by the Russian Science Foundation under Grant 24-29-00753.

Data Availability Statement: The original contributions presented in this study are included in the article. Further inquiries can be directed to the corresponding author.

Conflicts of Interest: The authors declare no conflicts of interest.

Glossary

List of Abbreviations

CPSR	Constant power speed range
EESM	Electrically excited synchronous machine
EMF	Electromotive force
FOC	Field-oriented control
HESM	Harmonic Exciter Synchronous Machine
IM	Induction motor
PM	Permanent magnet
PMSM	Permanent magnet synchronous motor
PWM	Pulse-width modulation

List of Mathematical Symbols

$a1$	Height of the field winding coil, mm
$b1$	Width of the field winding coil, mm
i	Imaginary unit
I_0	Neutral wire current, ϕ
I_0^{ref}	Reference of the neutral wire current
I_a, I_b, I_c	Phase currents of the rotor rectifier, A
I_A, I_B, I_C	Stator phase currents, A
I_{aL}, I_{bL}	Phase currents of the harmonic winding, A
I_{dq}	Stator currents in the rotating coordinate system, A
I_{dq}^{ref}	Reference of dq current
I_{rms}	Phase armature current RMS, A
I_x	Field winding current, A

K	Logical flag of the rotary rectifier model state
p	Pole pair number
PF	Power factor
P_1	Input electric real power, W
P_2	Output mechanical power, W
r	Field winding resistance, Ohm
R	Stator phase resistance, Ohm
R_0^{inv}	Proportional gain of the PI controller of neutral current, Ohm
R_{dq}^{inv}	Proportional gain of the PI controller of dq current, Ohm
t	Time variable, s
U_a, U_b, U_c	Phase voltages the rotor rectifier, V
U_{dq}	Stator voltages in the rotating coordinate system, A
u_{dq}	Output of PI-voltage controller
U_{sh}	Harmonic winding neutral point voltage, V
U_x	Field winding voltage, V
V_{rms}	Line-to-line voltage RMS, V
z	Logical flag of the rotary rectifier model state
α	Rotor pole angular dimension, mechanical degrees
β	Angular distance between the slots of the harmonic winding, mechanical degrees
ΔU_{dq}	Correction for PI-voltage controller
ε	Voltage drop across one open diode, V
η	Efficiency, %
Φ_0	Zero-sequence flux linkage, Wb
Φ_a, Φ_b	Phase flux linkages of harmonic winding, Wb
Φ_{dq}	Stator flux linkages in the rotating coordinate system, Wb
Φ_x	Field winding flux linkage, Wb
Ω	Rotor mechanical angular frequency, radian per second, rad/s
\int_0	Integral gain of the PI controller of neutral current, Ohm
\int_{dq}	Integral gain of the PI controller of dq current, Ohm

References

- Dmitrievskii, V.; Prakht, V.; Valeev, E.; Paramonov, A.; Kazakbaev, V.; Anuchin, A. Comparative Study of Induction and Wound Rotor Synchronous Motors for the Traction Drive of a Mining Dump Truck Operating in Wide Constant Power Speed Range. *IEEE Access* **2023**, *11*, 68395–68409. [\[CrossRef\]](#)
- Prakht, V.; Dmitrievskii, V.; Kazakbaev, V.; Valeev, E.; Paramonov, A.; Anuchin, A. Assessment of the Feasibility of Using a Synchronous Homopolar Motor Instead of an Induction Motor in a Traction Drive with a Wide Constant Power Speed Range. *IEEE Open J. Veh. Technol.* **2024**, *5*, 950–966. [\[CrossRef\]](#)
- Dianov, A.; Anuchin, A. Offline Measurement of Stator Resistance and Inverter Voltage Drop Using Least Squares. *IEEE Access* **2023**, *11*, 17053–17065. [\[CrossRef\]](#)
- Kim, B.; Lee, J.; Jeong, Y.; Kang, B.; Kim, K.; Kim, Y. Development of 50 kW traction induction motor for electric vehicle (EV). In Proceedings of the 2012 IEEE Vehicle Power and Propulsion Conference, Seoul, Republic of Korea, 9–12 October 2012; pp. 142–147. [\[CrossRef\]](#)
- Zhu, Z.Q.; Chu, W.Q.; Guan, Y. Quantitative comparison of electromagnetic performance of electrical machines for HEVs/EVs. *CES Trans. Electr. Mach. Syst.* **2017**, *1*, 37–47. [\[CrossRef\]](#)
- Sharp, A.; Monir, S.; Day, R.J.; Vagapov, Y.; Dianov, A. A Test Rig for Thermal Analysis of Heat Sinks for Power Electronic Applications. In Proceedings of the 2023 IEEE East-West Design & Test Symposium (EWDTS), Batumi, Georgia, 22–25 September 2023; pp. 1–4. [\[CrossRef\]](#)
- Ali, Y.; Kulik, E.; Anuchin, A.; Do, D.H. Thermal Cycling Effect in a Traction Inverter for Star-connected and Open-end Winding Permanent Magnet Synchronous Motors with Nearly Constant Losses Current Regulation. In Proceedings of the 2022 29th International Workshop on Electric Drives: Advances in Power Electronics for Electric Drives (IWED), Moscow, Russian, 26–29 January 2022; pp. 1–6. [\[CrossRef\]](#)
- Doerr, J.; Fröhlich, G.; Stroh, A. The Electric Drivetrain with Three-motor Layout of the Audi E-tron S. *MTZ Worldw.* **2020**, *81*, 16–25. [\[CrossRef\]](#)

9. Popescu, M.; Goss, J.; Staton, D.A.; Hawkins, D.; Chong, Y.C.; Boglietti, A. Electrical Vehicles—Practical Solutions for Power Traction Motor Systems. *IEEE Trans. Ind. Appl.* **2018**, *54*, 2751–2762. [CrossRef]
10. BMW Group. The First-Ever BMW iX3, PressClub Global, Article. Available online: <https://www.press.bmwgroup.com/global/article/detail/T0310696EN/the-first-ever-bmw-ix3?language=enhttps://www.netcarshow.com/bmw/2021-ix3/> (accessed on 2 January 2025).
11. Renault Fluence, Z.E. Is a Positive Influence. 2012. Available online: <https://www.torque.com.sg/reviews/renault-fluence-z-e-is-a-positive-influence/> (accessed on 2 January 2025).
12. Noeland, J.; Nuzzo, S.; Tessarolo, A.; Alves, E. Excitation System Technologies for Wound-Field Synchronous Machines: Survey of Solutions and Evolving Trends. *IEEE Access* **2019**, *7*, 109699–109718. [CrossRef]
13. Maier, M.; Parspour, N. Operation of an Electrical Excited Synchronous Machine by Contactless Energy Transfer to the Rotor. *IEEE Trans. Ind. Appl.* **2018**, *54*, 3217–3225. [CrossRef]
14. Illiano, E. Design of a Highly Efficient Brushless Current Excited Synchronous Motor for Automotive Purposes. Ph.D. Thesis, ETH-Zürich, Zurich, Switzerland, 2014. [CrossRef]
15. Boldea, I.; Andreescu, G.; Rossi, C.; Pilati, A.; Casadei, D. Active Flux Based Motion-Sensorless Vector Control of DC-Excited Synchronous Machines. In Proceedings of the 2009 IEEE Energy Conversion Congress and Exposition, San Jose, CA, USA, 20–24 September 2009; pp. 2496–2503. [CrossRef]
16. AHLE Develops Highly Efficient Magnet-Free Electric Motor. Press Release. Available online: <https://www.mahle.com/en/news-and-press/press-releases/mahle-develops-highly-efficient-magnet-free-electric-motor--82368> (accessed on 2 January 2025).
17. Dmitrievskii, V.; Prakht, V.; Kazakbaev, V. Traction Synchronous Machine with Rotor Field Winding and Controlled Magnetic Anisotropy. In Proceedings of the 2024 International Conference on Industrial Engineering, Applications and Manufacturing (ICIEAM), Sochi, Russian, 20–24 May 2024; pp. 512–517. [CrossRef]
18. Bukhari, S.S.H.; Memon, A.A.; Madanzadeh, S.; Sirewal, G.J.; Doval-Gandoy, J.; Ro, J.-S. Novel Single Inverter-Controlled Brushless Wound Field Synchronous Machine Topology. *Mathematics* **2021**, *9*, 1739. [CrossRef]
19. Bukhari, S.S.H.; Mangi, F.H.; Sami, I.; Ali, Q.; Ro, J.-S. High-Harmonic Injection-Based Brushless Wound Field Synchronous Machine Topology. *Mathematics* **2021**, *9*, 1721. [CrossRef]
20. Jong-seok, N.; Sabir, S.; Bukhari, H. Single-Inverter-Controlled Brushless Technique for Wound Rotor Synchronous Machines. KR Patent 20230075074A, 22 November 2021. Available online: <https://patents.google.com/patent/KR20230075074A> (accessed on 2 January 2025).
21. Humza, M.; Yazdan, T.; Ali, Q.; Cho, H.-W. Brushless Operation of Wound-Rotor Synchronous Machine Based on Sub-Harmonic Excitation Technique Using Multi-Pole Stator Windings. *Mathematics* **2023**, *11*, 1117. [CrossRef]
22. Prakht, V.; Dmitrievskii, V.; Kazakbaev, V.; Paramonov, A. Electrical. Machine. Patent Application RU 2024117933, 28 June 2024.
23. Zulqarnain, M.; Hammad, S.Y.; Ikram, J.; Bukhari, S.S.H.; Khan, L. Torque Ripple Reduction in Brushless Wound Rotor Vernier Machine Using Third-Harmonic Multi-Layer Winding. *World Electr. Veh. J.* **2024**, *15*, 163. [CrossRef]
24. Hargreaves, P.A.; Mecrow, B.C.; Hall, R. Calculation of Iron Loss in Electrical Generators Using Finite-Element Analysis. *IEEE Trans. Ind. Appl.* **2012**, *48*, 1460–1466. [CrossRef]

Disclaimer/Publisher’s Note: The statements, opinions and data contained in all publications are solely those of the individual author(s) and contributor(s) and not of MDPI and/or the editor(s). MDPI and/or the editor(s) disclaim responsibility for any injury to people or property resulting from any ideas, methods, instructions or products referred to in the content.